Journal of Alloys and Compounds 1022 (2025) 179828

Contents lists available at ScienceDirect

Journal of Alloys and Compounds

journal homepage: www.elsevier.com/locate/jalcom

# Effect of Er-doping on the macroscopic plasticity and shear band nucleation kinetics of CuZr-based metallic glass

Y.H. Gao [a,b,1], Y.Y. Sun [b,1], M.C. Jian [b], Y.B. Wang [b], Y. Huang [b], F.C. Wang [b], L. Fu [b], M.C. Li [a,*], C. Kursun [c], Y. Zhang [b], J.T. Huo [b], J.Q. Wang [b,*], M. Gao [b,*]

[a] School of Materials Science and Engineering & Xinjiang Engineering Research Center of Environmental and Functional Materials, Xinjiang University, Urumqi, Xinjiang 830046, China

[b] CAS Key Laboratory of Magnetic Materials and Devices, and Zhejiang Province Key Laboratory of Magnetic Materials and Application Technology, Ningbo Institute of Materials Technology and Engineering, Chinese Academy of Sciences, Ningbo 315201, China

[c] Kahramanmaras Sutcu Imam University, Faculty of Science, Departmant of Physics, Avsar Campus, Onikisubat 46100, Kahramanmaras, Türkiye

ARTICLE INFO

*Keywords:*
Minor alloying
Plasticity
First pop-in event
Shear band nucleation
Metallic glass

ABSTRACT

Minor alloying represents a commonly - employed experimental approach for adjusting the mechanical properties of metallic glasses. However, the physical mechanism underlying the minor alloying effect remains ambiguous due to the unknown atomic structure. In this study, we systematically investigated the minor alloying effect on the macroscopic plasticity of metallic glasses from the perspective of shear band nucleation kinetics. By taking $(Cu_{0.47}Zr_{0.45}Al_{0.08})_{100-x}Er_x$ (x = 0–4 at%) system as the research object, we determined the evolutions of plasticity, shear band nucleation kinetics including nucleation site density, nucleation rate, and activation barrier with varying Er doping contents. It was found that the optimal plasticity occurs when the Er element addition is 2 %, concurrent with the highest nucleation site density, the largest nucleation rate, and the lowest nucleation barrier. Furthermore, a scheme was introduced to illustrate the effects of Er doping on the plasticity and shear band nucleation kinetics of metallic glasses. The current study offers a novel perspective for understanding the correlation between chemical composition and deformation mechanism in amorphous materials.

## 1. Introduction

Metallic glasses (MGs), as a typical amorphous material, have drawn great attention because of their unique structure and outstanding properties, which hold substantial research significance and great potential for engineering applications [1–5]. One of the main sources of the immense appeal of MGs is their range of outstanding mechanical properties, such as high strength, great hardness, high elastic strain limit, high fracture toughness and remarkable wear resistance [6–9]. However, due to the lack of the intrinsic structural defects, MGs display the limited plastic deformation ability under external loading [6,10–12], which seriously restrains the practical applications as the structural materials. To overcome this bottleneck, a large number of researchers put forward a series of experimental methods, such as the introduction of second crystalline phases [13–15], the rejuvenation treatment [16,17], the regulation of the atomic structure [18,19], the surface treatment [20,21], and the chemical composition tuning [22–24]. Among these strategies, the minor-alloying method displays the flexible and convenient characteristics for adjusting the mechanical properties including the plastic deformation ability in MGs. Most of brittle MGs can be improved to a certain extent by appropriate minor alloying [24–26]. However, the physical mechanism for the minor-alloying effect on the plastic deformation ability is still unclear.

Different from the crystalline alloys, the mechanical behaviors of MGs are usually governed by one type of local deformation unit, shear band (SB) [6,26–28]. The initiation of an SB marks the onset of plastic yielding corresponding to the highly localized plastic flow, which limits ductility and leads to strain softening. The number of SBs and the propagation speed for SBs usually determine the detailed deformation behaviors. For MGs, the more SBs and the lower SB propagates, the better the plastic deformation ability. Considering that the formation and evolution of SBs during deformation are governed by their nucleation kinetics [29,30], the information on SB nucleation kinetics, including the nucleation sites, nucleation site density, nucleation rate

* Corresponding authors.
*E-mail addresses:* limingcan@xju.edu.cn (M.C. Li), jqwang@nimte.ac.cn (J.Q. Wang), gaomeng@nimte.ac.cn (M. Gao).
[1] These authors contributed equally to this work.

https://doi.org/10.1016/j.jallcom.2025.179828
Received 15 November 2024; Received in revised form 15 February 2025; Accepted 16 March 2025
Available online 19 March 2025

and nucleation barrier, is critical to reveal the deformation mechanism in MGs. Yet, in view of the stochastic nature of the SB nucleation, it is difficult to detect the nucleation information by traditional mechanical testing methods. Recently, one experimental framework by combining the nanoindentation testing with classical nucleation theory was advanced to quantitatively obtain the information of SB nucleation kinetics [31–34]. The effects of relaxation types, structural relaxation, strain rate on the SB nucleation behaviors and the ductility have been investigated, which indicates that this method is effective. Thus, the aspect of the SB nucleation kinetics may be used to reveal the underlying microscopic mechanism of the minor alloying effect on the macroscopic plasticity of MGs [35].

In this work, one known MG system of $Cu_{47}Zr_{45}Al_8$ was chosen as the research object considering its good glass formation ability and potential practical applications [35,36]. Previous research reported that the doping of rare earth elements can effectively improve the glass formation ability, the thermal stability and the plastic deformation ability [37–39]. Here, we selected one rare earth element of Er with low cost to investigate the minor alloying effects on the macroscopic plasticity and the SB nucleation kinetics of $(Cu_{0.47}Zr_{0.45}Al_{0.08})_{100-x}Er_x$ (x = 0–4, at%). The structure, the macroscopic mechanical properties, the SB nucleation kinetics involving the kind of SB nucleation site, the density of nucleation sites, the nucleation rate and the nucleation barrier were systematically investigated. Finally, the correlation between the different contents of Er-doping and the plastic deformation ability was revealed in terms of the SB nucleation kinetics.

## 2. Experimental methods

Alloy ingots with the nominal compositions of $(Cu_{0.47}Zr_{0.45}Al_{0.08})_{100-x}Er_x$ (x = 0–4, at%) were produced by means of arc melting technology under the condition of a high-purity argon atmosphere. The purity of the applied element metals of Cu, Zr, Al, and Er was 99.9 %. In order to attain chemical homogeneity, each alloy ingot was melted over six times. As soon as the alloy ingots had been prepared, they were broken into small pieces. Then, for every alloy ingot, the samples in the form of cylindrical rods with a diameter of 3 mm were prepared through suction casting into one water-cooled copper mold within an argon atmosphere. X-ray diffraction was employed to identify the amorphous nature of the as-cast rod-like samples (XRD, Bruker D8 Advance, Cu-Kα).

To quantitatively characterize the plastic deformation ability, with an Instron testing machine (Zwick/Roell Z100), the uniaxial compression tests were executed at room temperature. Following the standard ASTM (American Society for Testing and Materials) standard, the specimens for uniaxial compression tests were set as a height-to-diameter ratio of 2 (the diameter is 3 mm and the length is 6 mm) and the applied strain rate was 0.001 $s^{-1}$ . For each composition, at least three samples were applied for the compression tests to ensure repeatability and reliability. Before the tests, all of the rod specimens were polished carefully by a series of sand papers to avoid the influence of the surface morphology. After compression tests, the fracture surface morphology was observed using a scanning electron microscope (SEM, EVO18).

For characterization of SB nucleation kinetics, the nanoindentation tests were applied. Firstly, for every MG composition, the rod samples prepared beforehand were sliced into uniformly thin slices that were 1 mm in thickness. Second, all of the thin slices were initially polished to confirm the flat surface and then were mounted into rubber molds using a mixture of epoxy hardener and epoxy resin, followed by curing for 24 hours. In the final step, all of the mounted samples were progressively polished by means of diamond abrasive films having particle sizes of 30, 15, 6, 3, 1, 0.5, and 0.1 μm, respectively. During the final polishing stage, the chemo-mechanical polishing procedure with colloidal silica was used for additional polishing by combining mechanical polishing and etching effects. Once the polishing procedure was completed, all of the samples were left to stay at room temperature for four weeks so as to get rid of the residual surface stress. Then, a series of nanoindentation experiments were conducted with the help of a Hysitron TI950 nanoindenter that has a spherical tip with an effective radius of approximately 1.10 μm (Bruker). The nanoindentation experiments were performed under load-controlled mode and the applied loading rate was 0.2 mN/s. To ensure the statistical significance of the results, over 200 repetitions were conducted for each MG composition. The spacing of 20 μm was applied between the indentation points to prevent potential overlap of the strain fields between adjacent indents.

## 3. Results and discussion

### 3.1. Characterization of structure and macroscopic mechanical properties of $(Cu_{0.47}Zr_{0.45}Al_{0.08})_{100-x}Er_x$ (x = 0–4, at%) MGs

For the prepared 3 mm rod-like samples of $(Cu_{0.47}Zr_{0.45}Al_{0.08})_{100-x}Er_x$ (x = 0–4, at%) (the right part of Fig. 1(a)), the corresponding XRD patterns were shown in Fig. 1(b). For simplicity, these samples were marked as Er0, Er1, Er2, Er3 and Er4, respectively. Clearly, all of the rod samples are amorphous, which indicates that the Er doping is good for the glass formation. According to the mixing enthalpy criterion for glass formation, the values of the Er and Cu, Al are negative (the left part in Fig. 1(a)), which is beneficial to the glass formation ability [40,41].

To quantitatively characterize the macroscopic mechanical properties of $(Cu_{0.47}Zr_{0.45}Al_{0.08})_{100-x}Er_x$ (x = 0–4, at%) MGs, a series of uniaxial compression tests were performed with the strain rate of $1 \times 10^{-3}$ $s^{-1}$. The detailed compression stress and strain curves were displayed in Fig. 1(c). From the above curves, the values of the yield strength, the plastic strain and the elastic modulus can be determined and were listed in Table 1. At least three samples for each MG composition were applied for the uniaxial compression tests and the corresponding error bars for the above mechanical properties were also included in Table 1. One can see that different contents of Er doping make $(Cu_{0.47}Zr_{0.45}Al_{0.08})_{100-x}Er_x$ exhibit different mechanical behaviors. Firstly, for the elastic modulus, there appears the non-monotonic evolution with the increase of the content of the doped Er. When the Er concentration increases from 0 % to 2 %, the elastic modulus decreases; when the Er concentration further increases from 2 % to 4 %, the elastic modulus increases. At 2 %, the elastic modulus reaches the minimum value. This result is consistent with previous research [24–26]. Considering that the doping of the rare earth elements changes the atomic structure and the electronic structure, more related research needs to be conducted, which will be included in our future research plan. Secondly, for the adjustment of macroscopic plasticity, there is almost no plasticity (only 0.21 %) for $Cu_{0.47}Zr_{0.45}Al_{0.08}$ MG without Er doping. With the Er content increasing into 1 %, there appears one small plasticity (3.61 %). When the Er content increases into 2 %, the plastic strain is the largest (5.76 %). With the further increase of the Er content, the plastic deformation ability becomes weak, accompanied by a reduction in strength. And the plasticity is the smallest for $(Cu_{0.47}Zr_{0.45}Al_{0.08})_{96}Er_4$ MG (0.23 %). The comprehensive comparison of the plastic deformation ability and the strength was shown in Fig. 1(d). Thus, the $(Cu_{0.47}Zr_{0.45}Al_{0.08})_{98}Er_2$ MG displays the best comprehensive mechanical performance.

To further investigate the deformation mechanism during uniaxial compression for $(Cu_{0.47}Zr_{0.45}Al_{0.08})_{100-x}Er_x$ (x = 0–4, at%) MGs, the corresponding fracture surface morphologies were observed and displayed in Figs. 2(a)-2(e). From Figs. 2(a)-2(e), the main fracture morphology for all MG samples is the vein-like pattern, which is the typical character of the shear-governed deformation [42,43]. The difference lies in the size and density of the vein patterns. The comparison plot of the average size and density of the vein morphologies for different MGs was shown in Fig. 2(f). Obviously, the $(Cu_{0.47}Zr_{0.45}Al_{0.08})_{98}Er_2$ MG displays the smallest and most vein patterns, which implies that there appears the serious plastic deformation. In contrast, the $Cu_{0.47}Zr_{0.45}Al_{0.08}$ and $(Cu_{0.47}Zr_{0.45}Al_{0.08})_{96}Er_4$ MGs with poor plastic deformation ability display the largest but

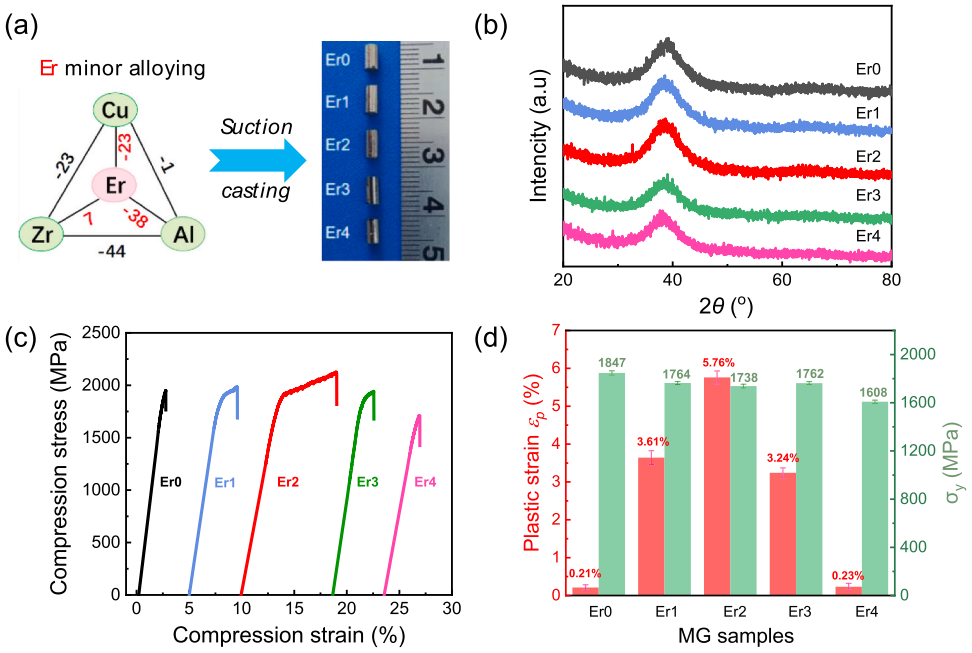


**Fig. 1.** (a) Designing strategy for Er-doped $(Cu_{0.47}Zr_{0.45}Al_{0.08})_{100-x}Er_x$ (x = 0–4, at%) MG systems. The right part gives the optical photos for the corresponding rod-like samples (The diameters of rod-like samples are 3 mm). (b) XRD patterns of $(Cu_{0.47}Zr_{0.45}Al_{0.08})_{100-x}Er_x$ (x = 0–4, at%) MG samples. (c) Compressive stress and strain curves of $(Cu_{0.47}Zr_{0.45}Al_{0.08})_{100-x}Er_x$ (x = 0–4, at%) MG rods. The strain rate is 0.001 $s^{-1}$. (d) Comparison of plastic strain and yield strength for $(Cu_{0.47}Zr_{0.45}Al_{0.08})_{100-x}Er_x$ (x = 0–4, at%) (x = 0–4, at%) MG rods.

**Table 1**
Data list of elastic modulus, yield strength, and plastic strain for $(Cu_{0.47}Zr_{0.45}Al_{0.08})_{100-x}Er_x$ (x = 0–4, at%) MGs.

| Samples | Elastic modulus (GPa) | Yield strength (MPa) | Plastic strain (%) |
|---|---|---|---|
| Er0 | 98.23 ± 0.92 | 1847 ± 18 | 0.21 ± 0.07 |
| Er1 | 98.73 ± 0.68 | 1764 ± 12 | 3.61 ± 0.18 |
| Er2 | 84.21 ± 0.75 | 1738 ± 15 | 5.76 ± 0.17 |
| Er3 | 91.67 ± 0.65 | 1762 ± 13 | 3.24 ± 0.13 |
| Er4 | 104.86 ± 0.85 | 1608 ± 16 | 0.23 ± 0.09 |

fewest vein pattern. Therefore, the above results and discussions show that the appropriate doping of the Er element (2 %) can effectively improve the macroscopic plasticity of Cu-Zr-Al MG system. Taking into account that the mechanical behaviors of MGs are mainly controlled by the formed SBs during deformation, the SB nucleation kinetics behaviors are of great importance for understanding the Er minor alloying effect on the macroscopic mechanical properties. The detailed SB nucleation kinetics analyses are described in the below.

### *3.2. SB nucleation kinetics for $(Cu_{0.47}Zr_{0.45}Al_{0.08})_{100-x}Er_x$ (x = 0–4, at%) MGs*

#### *3.2.1. SB nucleation process and nucleation site types*

Under uniaxial loading, the nucleation process of SBs is difficult to be observed by the traditional compression tests due to its stochastic nature and weak signal. In contrast, the nanoindentation platform with high spatial resolution and signal sensitivity provides a flexible tool to detect the SB nucleation kinetics [31–34]. Here, by taking $Cu_{47}Zr_{45}Al_8$ MG sample as an example, the detailed analyses process will be displayed. As depicted in Fig. 3(a), a typical load-displacement curve for nanoindentation with a loading rate of 0.2 mN/s for $Cu_{47}Zr_{45}Al_8$ MG is illustrated. When undergoing nanoindentation, the material at first shows an elastic Hertzian response, as depicted by the blue dashed curve in Fig. 3(a). The first pop-in occurrence, which is marked by the red circle in Fig. 3(a), is witnessed as a sudden rise in displacement under a steady load. It has been confirmed by previous studies that the nucleation process of SBs is corresponding to the first pop-in event [31–34,44]. Therefore, by analyzing a large number of first pop-in events with statistical significance, the SB nucleation kinetics associated with different MGs can be gotten.

For ensuring the statistical significance, approximately 200 individual nanoindentation measurements for each MG sample were conducted and the load values of a great deal of first pop-in events were collected, as shown in Fig. 3(b). One can see that there is no systematic drift for all of the SB nucleation events, indicating that SB nucleation is a random process. Based on the load distribution of the first pop-in loads, the normalized cumulative distributions of the first pop-in loads for $(Cu_{0.47}Zr_{0.45}Al_{0.08})_{100-x}Er_x$ (x = 0–4, at%) MGs were acquired and presented in Fig. 3(c). For different Er-doped MGs, there appear different shifts of the cumulative distributions compared to that of $Cu_{47}Zr_{45}Al_8$ MG. To better illustrate the variation of loads for SB nucleation, the first pop-in load values where the normalized cumulative distribution value is 0.5 were plotted in Fig. 3(d). Evidently, as the doped Er content rises, the load at the first pop-in event first declines and then goes up. At the 2 % Er content, the first pop-in load reaches the minimum value, which implies that the SB nucleation for 2 % doped MG sample is easiest.

To identify the SB nucleation site types for different MGs, the 3D probability distribution function of the first pop-in loads according to the results in Fig. 3(c) was shown in Fig. 3(e). From Fig. 3(e), a distinct shoulder appears on the high-load side of the peak for all MG samples, rather than following a typical symmetric Gaussian function. What is more, even though the probability density distributions show similar asymmetric characteristics, the asymmetry of the MG samples varies because of the different positions of the shoulders. This special distribution character indicates that there exist two different SB nucleation sites being activated within different load ranges. To simplify matters, we labeled the two SB nucleation sites as low-load sites and high-load sites respectively. To quantitatively show the progression of the two SB nucleation sites along with the alteration of Er content, the peak values of the probability density functions regarding the two sites were exhibited in Fig. 3(f). Evidently, the peak values of the probability density for the two SB nucleation sites at first increase, then decrease, and reach their highest point in the 2 % Er-doped MG. The above results

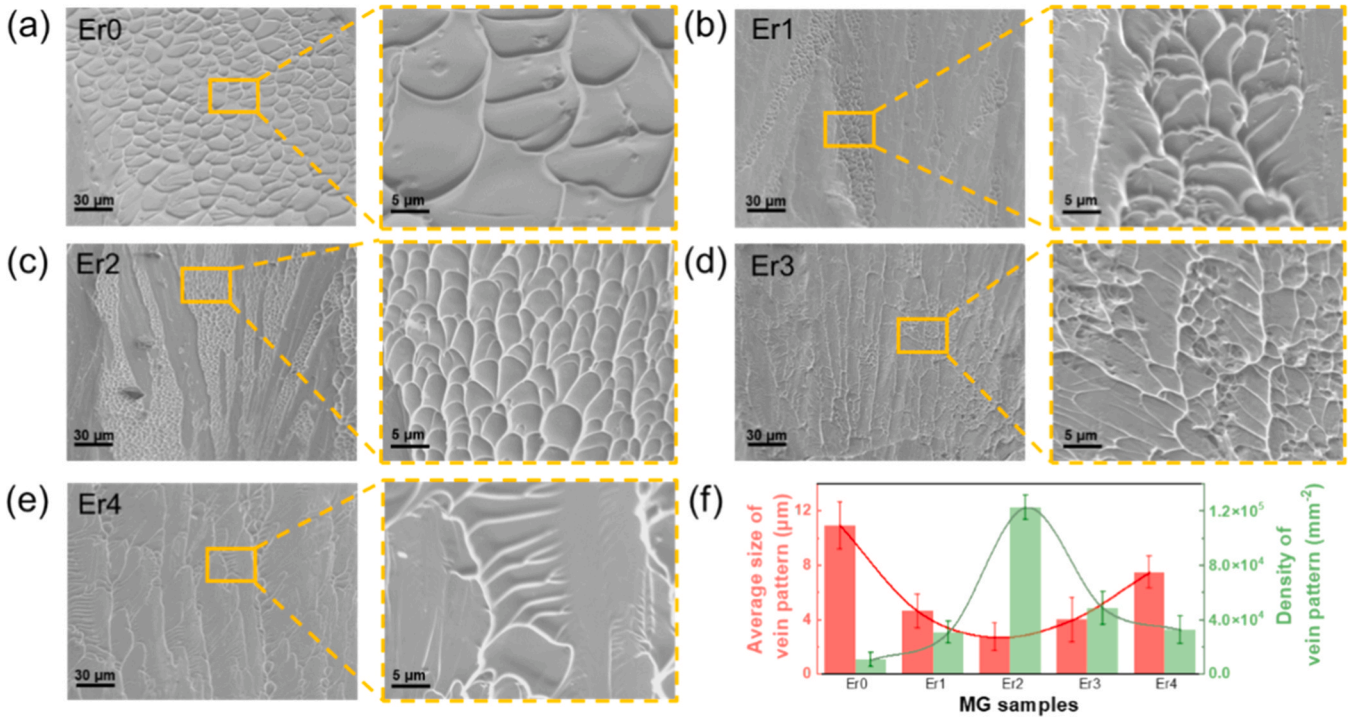


**Fig. 2.** (a-e) SEM images of the whole fracture surface morphologies (left) and the typical fracture features (right) for $(Cu_{0.47}Zr_{0.45}Al_{0.08})_{100-x}Er_x$ (x = 0–4, at%) MG rods. (f) Comparison of the average size and density of vein fracture patterns for $(Cu_{0.47}Zr_{0.45}Al_{0.08})_{100-x}Er_x$ (x = 0–4, at%) MG rods.

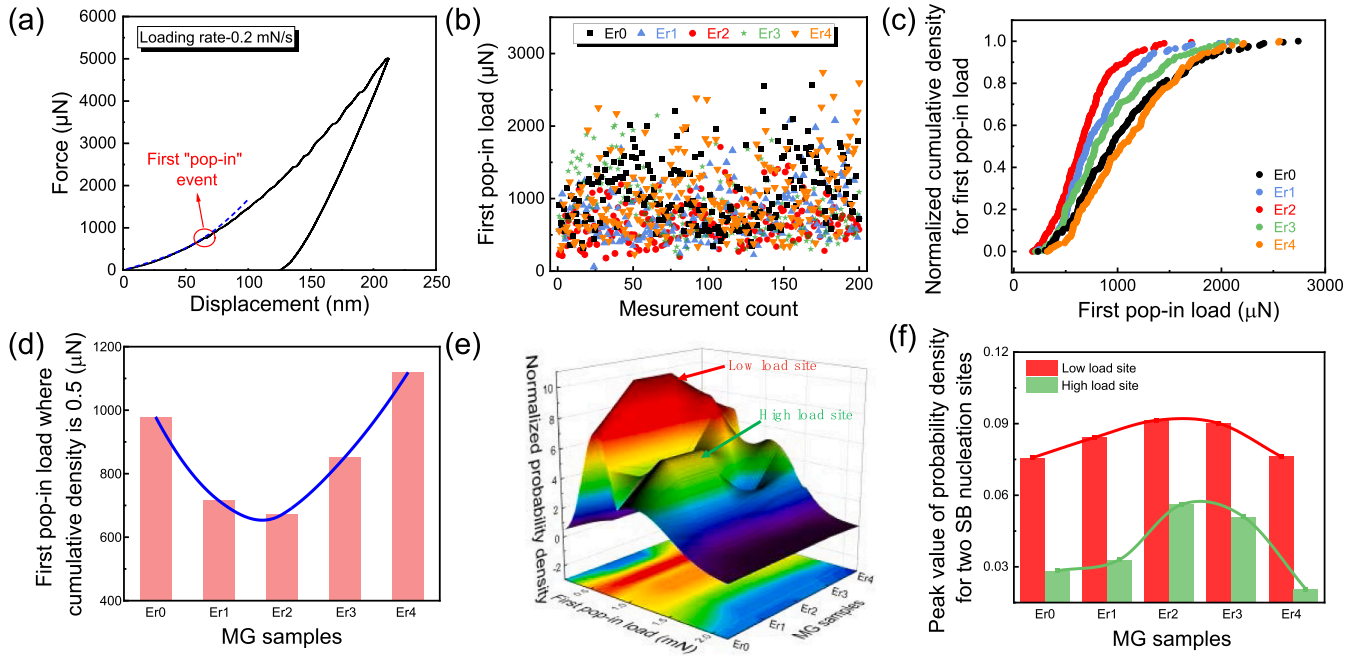


**Fig. 3.** (a) Nanoindentation displacement-load curve with a loading rate of 0.2 mN/s for $Cu_{47}Zr_{45}Al_8$ MG sample. The red circle marks the first pop-in event and the blue dashed curve gives the fitted Herzian function. (b) First pop-in load distributions for $(Cu_{0.47}Zr_{0.45}Al_{0.08})_{100-x}Er_x$ (x = 0–4, at%) MGs. For each MG, the distribution analysis was based on about 200 independent nanoindentation tests. (c) Normalized cumulative densities of first pop-in events for $(Cu_{0.47}Zr_{0.45}Al_{0.08})_{100-x}Er_x$ (x = 0–4, at%) MGs. (d) First pop-in load values for $(Cu_{0.47}Zr_{0.45}Al_{0.08})_{100-x}Er_x$ (x = 0–4, at%) MGs when the cumulative density value is 0.5. (e) Three dimensional wiremesh mapping as a function of load and length at first pop-in events for $(Cu_{0.47}Zr_{0.45}Al_{0.08})_{100-x}Er_x$ (x = 0–4, at%) MGs. (f) Peak values of probability density for two different SB nucleation sites for $(Cu_{0.47}Zr_{0.45}Al_{0.08})_{100-x}Er_x$ (x = 0–4, at%) MGs.

imply that both of two SB nucleation sites for $Cu_{47}Zr_{45}Al_8$ MG can be easier to be activated than those of other MG samples, which agrees with the results shown in Fig. 3(d). In the following sections, we will discuss the nucleation site densities, nucleation rates, and nucleation barriers of SBs with different Er doped contents. In addition, it should be pointed out that the feature of dual-peak SB nucleation sites for MGs is common and is independent of both energy states and chemical composition [31, 34]. However, MGs having varying compositions show highly different

SB nucleation behaviors, thereby causing diverse mechanical properties.

### 3.2.2. SB nucleation site density

For MGs, the more of SB nucleation sites are activated during deformation, the more SBs form [6]. More formed SBs are favorable to undertake more external loading and display the better plastic deformation ability. Therefore, the density of SB nucleation sites is an important parameter for comprehending the effect of minor alloying on the mechanical behaviors of MGs. Previous reports have indicated that the SB nucleation is stochastic and there are no orientation-dependent nucleation events in MGs [27–29]. Thus, herein, we presume that the activated SB nucleation sites are randomly dispersed within the deformation volume $V_{def}$. A series of our previous works also verified that this assumption is reasonable and effective for describing and simulating the SB nucleation behaviors of MGs [32–35]. During nanoindentation tests, the volume of deformation $V_{def}$ under external load usually follows the minimum criterion of the volume of the pop-in event [45,46]. Thus, $V_{def}$ can be regarded as approximately $1\,\%V_{dis}$, with $V_{dis}$ being the displacement volume right beneath the indenter tip [44]. The $V_{dis}$ is given by

$$V_{dis} = \frac{\pi}{6}\left[3\left(\frac{9P^2R^5}{16E_r^2}\right)^{\frac{1}{3}} + \frac{9P^2}{16E_r^2R}\right] \tag{1}$$

in which $P$ represents the applied load; $R$ stands for the tip radius of the indenter; $E_r$ denotes the reduced modulus, $E_r = \frac{E_sE_i}{E_i\left(1-\nu_s^2\right)+E_s\left(1-\nu_i^2\right)}$, where $E_s$ and $E_i$ are the elastic modulus for the MG samples and the indenter; $\nu_s$ and $\nu_i$ are the Poisson's ratio for the MG samples and the indenter [32]. For the applied indenter in this work, the modulus $E_i$ is 1141 GPa, the Poisson's ratio $\nu_i$ is 0.07 and the tip radius $R$ is 100 nm. For $(Cu_{0.47}Zr_{0.45}Al_{0.08})_{100-x}Er_x$ (x = 0–4, at%) MG samples, the modulus $E_s$ can be ascertained through nanoindentation, and the specific values of $E_s$ were listed in Table 1. For MGs, the Poisson's ratio is insensitive to the minor addition of the rare earth elements [25]. Here, for $(Cu_{0.47}Zr_{0.45}Al_{0.08})_{100-x}Er_x$ (x = 0–4, at%) MG samples, the difference of Poisson's ratio can be considered as being negligible. The values of the Poisson's ratio for all of MGs are about 0.364 [47].

After confirming the deformation volume during nanoindentation, the density of the SB nucleation site $s$ can be described as the proportion of the number of nucleation sites to the deformed volume. For experimental estimation, it is not easy to acquire the quantitative data about the number of nucleation sites. On the other hand, taking into account the probability density of the SB nucleation sites $W$ can be expressed by

$$W = 1 - \exp\left(-sV_{def}\right) \tag{2}$$

Thus, it is feasible to obtain the detailed information regarding the nucleation site density. Here, from the experimental results of the first pop-in events, the detailed evolution of $W$ with different external loads can be obtained from Fig. 3(e). Thus, the densities of the nucleation sites for two distinct nucleation sites can be acquired from Eq. (2), and be expressed as

$$s = -\frac{1}{0.01 * \frac{\pi}{6}\left[3\left(\frac{9P^2R^5}{16E_r^2}\right)^{\frac{1}{3}} + \frac{9P^2}{16E_r^2R}\right]}\ln(1-W) \tag{3}$$

By taking the detailed values of the parameters into Eq. (3), the nucleation site density functions related to two nucleation sites were displayed in Fig. 4(a). It can be observed that various MG samples exhibit distinct SB nucleation density evolution trajectories in response to external loads. To further quantitatively study the effect of Er doping on SB nucleation site density, the density peak values of two nucleation sites can be determined from Fig. 4(a) and shown in Fig. 4(b). First, as the Er content increases, the peak values of both two nucleation sites initially increase and then decrease. At the Er doping content of 2 % Er, the nucleation site densities reach the maximum values, which means that $(Cu_{0.47}Zr_{0.45}Al_{0.08})_{98}Er_2$ MG has the most SB nucleation sites.

### 3.2.3. SB nucleation rate

Considering that the formation of SBs during deformation is a pro-

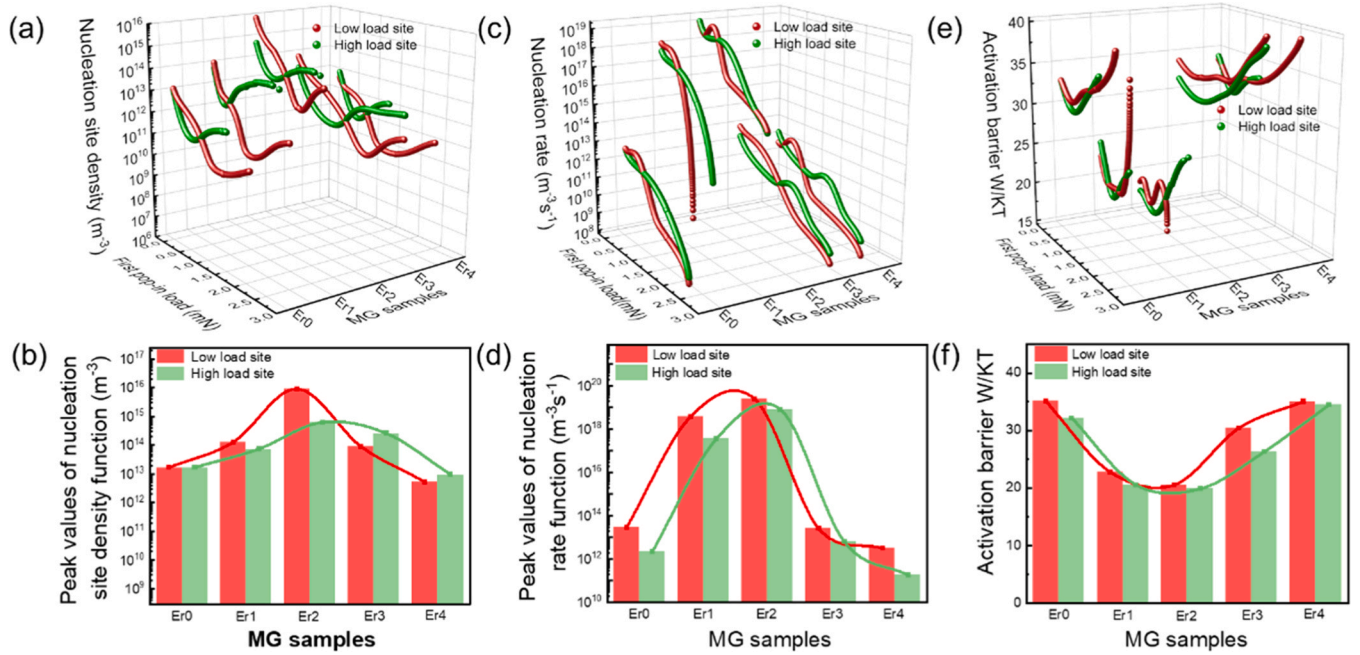


**Fig. 4.** (a) Three dimensional distribution of nucleation site densities of two SB nucleation sites for $(Cu_{0.47}Zr_{0.45}Al_{0.08})_{100-x}Er_x$ (x = 0–4, at%) MGs. (b) Peak values of nucleation side density functions for $(Cu_{0.47}Zr_{0.45}Al_{0.08})_{100-x}Er_x$ (x = 0–4, at%) MGs. (c) Three dimensional distribution of nucleation rates of two SB nucleation sites for $(Cu_{0.47}Zr_{0.45}Al_{0.08})_{100-x}Er_x$ (x = 0–4, at%) MGs. (d) Peak values of nucleation rate functions for $(Cu_{0.47}Zr_{0.45}Al_{0.08})_{100-x}Er_x$ (x = 0–4, at%) MGs. (e) Three dimensional distribution of the nucleation barriers of two SB nucleation sites for $(Cu_{0.47}Zr_{0.45}Al_{0.08})_{100-x}Er_x$ (x = 0–4, at%) MGs. (f) Peak values of nucleation barrier functions for $(Cu_{0.47}Zr_{0.45}Al_{0.08})_{100-x}Er_x$ (x = 0–4, at%) MGs.

cess of the nucleation and growth of the nucleation sites, the nucleation rate of SB nucleation sites is crucial for determining the number of formed SBs as well as the resulting mechanical behaviors [27,44]. Here, to obtain the nucleation rate from the first pp-in events in Fig. 3, we assume that the SB nucleation process follows the classical nucleation theory. Thus, by combining with Eqs. (1)-(3), one can obtain detailed information about the nucleation rate by following the steps described below. Firstly, according to the experimental results of the first pop-in events shown in Fig. 3(e), the kernel density function corresponding to the experimental probability density function $f(t)$ was introduced [31–34]. Subsequently, the cumulative distribution function $F(t)$ can be acquired by integrating the aforementioned kernel density function. After that, the statistical probability density function known as the hazard rate function $\lambda(t)$ can be computed in accordance with the equation $\lambda(t) = f(t)/[1 - F(t)]$ [32]. The hazard function can be employed to describe the likelihood of an event remaining in existence over time, which is directly related to the nucleation rate. As a result, the nucleation rate $J$ can be computed by

$$J = \lambda(t)/V_{def} \tag{4}$$

According to the Eq. (4) and the detailed experimental results in Fig. 3(e), the SB nucleation rate for two different nucleation sites $(Cu_{0.47}Zr_{0.45}Al_{0.08})_{100-x}Er_x$ (x = 0–4, at%) MGs can be obtained and shown in Fig. 4(c).

From Fig. 4(c), MGs with different Er doping contents display significantly different nucleation rate evolution behaviors with the loads. For all of MGs, the nucleation sites under low load are activated first, and the nucleation rate rises rapidly. Subsequently, when the load reaches one critical value, the nucleation site under high load begins to be activated, and the nucleation rate gradually exceeds that of the low load nucleation sites. To comprehensively compare the nucleation rate for different MGs, the peak values of the nucleation rate corresponding to the two nucleation sites in $(Cu_{0.47}Zr_{0.45}Al_{0.08})_{100-x}Er_x$ (x = 0–4, at%) MGs were acquired and plotted in Fig. 3(d). Evidently, the peak values of the nucleation rates for both of these nucleation sites show an initial upward trend followed by a downward trend as the Er doping content increases. At the Er doping content of 2 %, the nucleation rate peak values of two nucleation sites reach the maximum points. Compared to the nucleation rates of $Cu_{47}Zr_{45}Al_8$, $(Cu_{0.47}Zr_{0.45}Al_{0.08})_{97}Er_3$ and $(Cu_{0.47}Zr_{0.45}Al_{0.08})_{96}Er_4$, the nucleation rates for $(Cu_{0.47}Zr_{0.45}Al_{0.08})_{98}Er_2$ MG exhibit the nearly six to seven orders of magnitude larger, indicating that the Er doping has a particularly significant impact on the nucleation rate of the MGs. The greater the nucleation rate is, the more and faster the SBs will be formed, which helps to improve the plastic deformation ability of MGs. The above results and discussions are in line with the outcomes in Figs. 1(c) and 1(d) regarding the evolution of plasticity with the Er doping contents.

#### 3.2.4. SB nucleation barrier

Based on the cooperative shear deformation model proposed by W. L. Johnson and K. Samwer [48], the SB nucleation can be looked upon as an activation process under the influence of the external load $\tau$. Subsequently, the correlation between the nucleation rate $J$ and the nucleation activation barrier $W(\tau)$ can be formulated as

$$J = \omega \exp(-\frac{W(\tau)}{KT}) \tag{5}$$

in which $\omega$ represents the frequency constant and it is the result of multiplying an atomic jump frequency (for MGs, this can be regarded as $10^{13}$ $s^{-1}$) by the nucleation site density [34]. Then, according to Eq. (5), the SB nucleation activation barrier can be obtained by

$$W(\tau)/\ kT = \ln(\omega/\ J) \tag{6}$$

After taking the results of the nucleation rates in Fig. 4(c) into Eq. (6), the detailed nucleation activation barriers of two nucleation sites for $(Cu_{0.47}Zr_{0.45}Al_{0.08})_{100-x}Er_x$ (x = 0–4, at%) MGs were calculated and displayed in Fig. 4(e). Similar to the nucleation rates in Fig. 4(c), the nucleation activation barriers of two different nucleation sites for $(Cu_{0.47}Zr_{0.45}Al_{0.08})_{100-x}Er_x$ (x = 0–4, at%) MGs display different evolution behaviors with the external load. For the purpose of quantitatively characterizing the evolution behaviors, the peak values of the nucleation activation barriers corresponding to the two nucleation sites for $(Cu_{0.47}Zr_{0.45}Al_{0.08})_{100-x}Er_x$ (x = 0–4, at%) MGs were obtained from Fig. 4 (e) and shown in Fig. 4(f). Usually, the SB nucleation barrier can roughly describe the difficulty of SB nucleation events occurring during deformation. First, for the low load and high load nucleation sites, with the increase of the doped Er contents, the activation barriers firstly decrease and then increase. At the 2 % Er doping content, the activation barriers reach the minimum values, which indicates that the formation of SBs for $(Cu_{0.47}Zr_{0.45}Al_{0.08})_{98}Er_2$ MG is easiest. These results are consistent with the results in Fig. 1(c) and Fig. 4(d).

In addition, it should be noted that the difference in activation barriers for two nucleation sites seems not significant, indicating that the activation energy required for SB nucleation of two different sites is very close. Considering that two different nucleation sites are structurally originated from the intrinsic heterogeneous structure of MGs [49,50], the low load nucleation site and high load nucleation site can be considered to be activated from the liquid-like and solid-like regions at the nanoscale. The above results indicate that the intrinsic heterogeneous structure is actually affected by different Er doping contents. However, the difference of the properties between the liquid-like and solid-like regions for MGs may not be obviously changed considering the close values of the activation barriers for two nucleation sites.

### 3.3. Physical mechanism of the Er-doping effect on the macroscopic ductility and SB nucleation kinetics in MGs

Although there have been previous researchers focusing on the minor-alloying effects on the plasticity of MGs based on the free volume and shear transformation zone model [25,37–39,51,52], there is no research to clarify the correlation between the minor-alloying induced the brittle-ductile transition and the SB nucleation kinetics. Based on the results and discussions, different doping contents of the Er element actually have the significant influences on the macroscopic plasticity and the SB nucleation kinetics. Based on the results and discussions in the current work, different doping contents of the Er element actually have the significant influences on the macroscopic plasticity and the SB nucleation kinetics. The SB nucleation kinetics including the nucleation site density, the nucleation rate and the activation barrier display a positive correspondence with the macroscopic plasticity, that is, the higher of the site density, the faster of the SBs nucleate and the lower of the activation barrier, the better of the plastic deformation ability. On the other hand, the transition of the deformation mode between brittle and ductile is caused by the transition of the SB nucleation kinetics. Fig. 5 presents a scheme that clearly illustrates the physical mechanism underlying the influence of Er doping on the deformation mode and SB nucleation kinetics in MGs.

It should be noted that except for the Er doping, the minor alloying of other rare earth elements should have the similar effect on the improvement of mechanical properties in MGs. B.W. Zhou et al. found that Dy doping first enhances and then weakens the plasticity of the Cu-Zr-Al MG system [53], which is consistent with the results of our work. On the other hand, considering the differences of the atomic radius and the electronic structure, different rare earth elements should play different roles in mechanical behaviors of MGs. B. Huang et al. reported that as the atomic radius of the rare earth elements increases, the elastic modulus and strength tend to increase [54]. For the improvement of plasticity, only some rare earth elements have the positive effect. Thus, the detailed physical mechanism for the doping effect difference of different rare earth elements needs more researches to clarify, which is not the focus of the current work. Considering that the SB nucleation

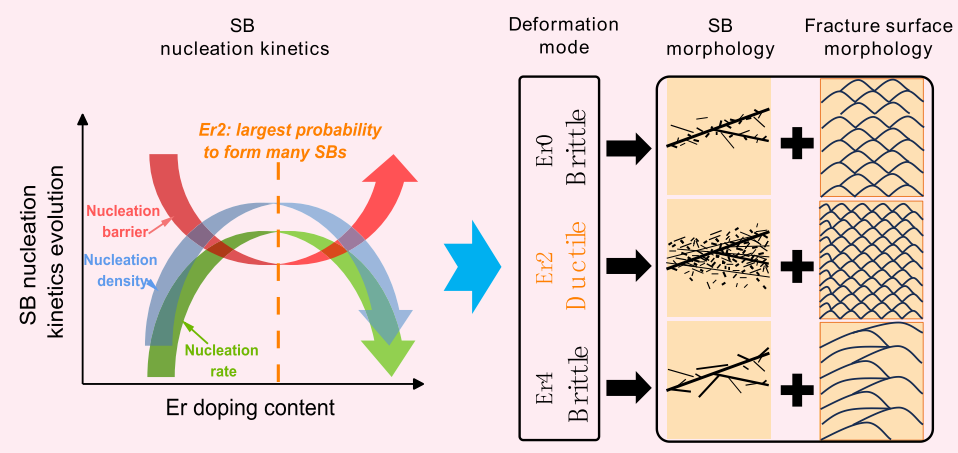


**Fig. 5.** Scheme of the Er-doping effect on SB nucleation kinetics and deformation behaviors.

kinetics is closely related to various mechanical properties, including plasticity, toughness, mechanical relaxation, and elastic modulus [31–34], it provides a new viewpoint for understanding the diverse mechanical behaviors and microscopic deformation mechanisms in different amorphous materials. On the other hand, although the minor alloying effect on the plasticity of MGs is well explained from the SB nucleation kinetics, how to choose the specific doping element and the proper doping content is still challenging. Our previous research has verified that different SB nucleation sites in MGs correspond to various structural heterogeneities, and nanoscale liquid-like regions are likely to generate SBs [33]. The connection between the minor doping element and the relevant structural heterogeneity holds the key to adjusting the SB nucleation kinetics and mechanical behaviors, and this will be the focus of our future research work.

## 4. Conclusions

In summary, we have systematically explored the effects of Er doping on the macroscopic mechanical behaviors and the detailed shear band (SB) nucleation kinetics, which encompasses the nucleation site density, nucleation rate, and nucleation barrier within the $Cu_{47}Zr_{45}Al_8$ MG. It was found that different Er doping contents arise the significant changes for both of the plasticity and nucleation kinetics. As the doped Er content rises from 0 % to 4 %, the deformation mode undergoes two transitions. When the Er concentration increases from 0 % to 2 %, the mode shifts from brittle to ductile, and when it increases from 2 % to 4 %, it changes from ductile to brittle. At 2 % Er doping, the optimal macroscopic plasticity is achieved. Significantly, at this 2 % Er doping level, the SB nucleation kinetics demonstrate that the nucleation site density and nucleation rate attain their maxima, while the nucleation barrier reaches its minimum. A positive relationship exists between the macroscopic plasticity and the SB nucleation kinetics. The current work not only presents a novel perspective for comprehending the influence of minor alloying on macroscopic mechanical behaviors but also motivates a new approach for adjusting mechanical properties. This novel strategy relies on the kinetic SB nucleation behavior at the nanoscale, rather than traditional average defects such as free volumes or shear transformation zones.

## CRediT authorship contribution statement

**Y. H. Gao:** Investigation, Methodology, Formal analysis, Resources, Writing - original draft. **Y. Y. Sun:** Methodology, Formal analysis, Resources, Writing - original draft. **M. C. Jian:** Formal analysis, Validation. **Y. B. Wang:** Formal analysis, Validation. **Y. Huang:** Methodology, Formal analysis. **F. C. Wang:** Validation. **L. Fu:** Validation. **M. C. Li:** Conceptualization, Funding acquisition, Supervision, Writing - review & editing. **C. Kursun:** Formal analysis. **Y. Zhang:** Validation. **J. T. Huo:** Funding acquisition, Validation. **J. Q. Wang:** Funding acquisition, Project administration, Writing - review & editing. **M. Gao:** Conceptualization, Funding acquisition, Supervision, Project administration, Resources, Writing - review & editing.

## Declaration of Competing Interest

The authors declare that they have no known competing financial interests or personal relationships that could have appeared to influence the work reported in this paper.

## Acknowledgements

This work was supported by the National Natural Science Foundation of China (52201194, 52261028, 52471187, 52222105, 92163108, 52231006), 3315 Innovation Youth Talent in Ningbo City (2021A123G), Youth Innovation Promotion Association CAS (No. 2019296), Zhejiang Provincial Natural Science Foundation of China (LR22E010004), Zhejiang Provincial Natural Science Foundation Regional Innovation and Development Joint Foundation with Quzhou City (LZY23E010002) and Natural Science Foundation of Xinjiang Uygur Autonomous Region of China (No. 2022D01C383).

## Data availability

Data will be made available on request.

## References

[1] W.H. Wang, C. Dong, C.H. Shek, Bulk metallic glasses, Mater. Sci. Eng. R. -Rep. 44 (2-3) (2004) 45–89.
[2] M. Telford, The case for bulk metallic glass, Mater. Today 7 (3) (2004) 36–43.
[3] A.L. Greer, E. Ma, Bulk metallic glasses at the cutting edge of metals research, MRS Bull. 32 (8) (2007) 611–619.
[4] M.W. Chen, A brief overview of bulk metallic glasses, NPG Asia Mater. 3 (9) (2011) 82–90.
[5] M.X. Li, S.F. Zhao, Z. Lu, A. Hirata, P. Wen, H.Y. Bai, M. Chen, J. Schroers, Y. Liu, W.H. Wang, High-temperature bulk metallic glasses developed by combinatorial methods, Nature 569 (7754) (2019) 99–103.
[6] A.L. Greer, M.B. Costa, O.S. Houghton, Metallic glasses, MRS Bull. 48 (2023) 1054–1061.
[7] C. Schuh, T. Hufnagel, U. Ramamurty, Mechanical behavior of metallic glasses, Acta Mater. 55 (12) (2007) 4067–4109.
[8] M.D. Demetriou, M.E. Launey, G. Garrett, J.P. Schramm, D.C. Hofmann, W. L. Johnson, R.O. Ritchie, A damage-tolerant glass, Nat. Mater. 10 (2) (2011) 123–128.
[9] J.J. Si, T. Wang, Y.D. Wu, Y.H. Cai, X.H. Chen, W.Y. Wang, Z.K. Liu, X.D. Hui, Cr-based bulk metallic glasses with ultrahigh hardness, Appl. Phys. Lett. 106 (2015) 251905.

[10] F.C. Li, M.X. Li, L.W. Hu, J.S. Cao, C. Wang, Y.T. Sun, W.H. Wang, Y.H. Liu, Achieving diamond-like wear in Ta-rich metallic glasses, Adv. Sci. 10 (2023) 2301053.
[11] Y. Zhang, W.H. Wang, A.L. Greer, Making metallic glasses plastic by control of residual stress, Nat. Mater. 5 (11) (2006) 857–860.
[12] S. Sohn, N. Liu, G.H. Yoo, A. Ochiai, J. Chen, C. Levitt, G. Liu, S.C. Schroers, E. T. Lund, E.S. Park, J. Schroers, A framework for plasticity in metallic glasses, Materialia 31 (2023) 101876.
[13] H. Wang, W. Dmowski, Y. Tong, Z. Wang, Y. Yokoyama, J. Ketkaew, J. Schroers, T. Egami, Nonaffine Strains Control Ductility of Metallic Glasses, Phys. Rev. Lett. 128 (15) (2022) 155501.
[14] Y. Wu, Y. Xiao, G. Chen, C.T. Liu, Z. Lu, Bulk metallic glass composites with transformation-mediated work-hardening and ductility, Adv. Mater. 22 (25) (2010) 2770–2773.
[15] D.C. Hofmann, J.Y. Suh, A. Wiest, G. Duan, M.L. Lind, M.D. Demetriou, W. L. Johnson, Designing metallic glass matrix composites with high toughness and tensile ductility, Nature 451 (7182) (2008) 1085–1089.
[16] X. Fu, G. Wang, Y. Wu, W. Song, C.H. Shek, Y. Zhang, J. Shen, R.O. Ritchie, Compressive ductility and fracture resistance in CuZr-based shape-memory metallic-glass composites, Int. J. Plast. 128 (2020) 102687.
[17] J. Pan, Y.X. Wang, Q. Guo, D. Zhang, A.L. Greer, Y. Li, Extreme rejuvenation and softening in a bulk metallic glass, Nat. Commun. 9 (1) (2018) 560.
[18] Z.Q. Ren, A.A. Churakova, X. Wang, S. Goel, S.N. Liu, Z.S. You, Y. Liu, S. Lan, D. V. Gunderov, J.T. Wang, R.Z. Valiev, Enhanced tensile strength and ductility of bulk metallic glasses Zr52.5Cu17.9Al10Ni14.6Ti5 via high-pressure torsion, Mater. Sci. Eng. A 803 (2021) 140485.
[19] Y. Wu, D. Cao, Y. Yao, G. Zhang, J. Wang, L. Liu, F. Li, H. Fan, X. Liu, H. Wang, X. Wang, H. Zhu, S. Jiang, P. Kontis, D. Raabe, B. Gault, Z. Lu, Substantially enhanced plasticity of bulk metallic glasses by densifying local atomic packing, Nat. Commun. 12 (1) (2021) 6582.
[20] H.K. Kim, J.C. Lee, Atomic-scale structures determining the plasticity of metallic glasses viewed from the icosahedral medium-range orders and its spatial distribution, Mater. Sci. Eng. A 894 (2024) 146198.
[21] B. Sarac, J. Schroers, Designing tensile ductility in metallic glasses, Nat. Commun. 4 (2013) 2158.
[22] M. Gao, J. Dong, Y. Huan, Y.T. Wang, W.H. Wang, Macroscopic tensile plasticity by scalarizating stress distribution in bulk metallic glass, Sci. Rep. 6 (2016) 21929.
[23] Y.H. Liu, G. Wang, R.J. Wang, D.Q. Zhao, M.X. Pan, W.H. Wang, Super Plastic Bulk Metallic Glasses at Room Temperature, Science 315(5817) 1385-1388.
[24] S. Hilke, H. Rösner, G. Wilde, The role of minor alloying in the plasticity of bulk metallic glasses, Scr. Mater. 188 (2020) 50–53.
[25] J. Chen, Y. Zhang, J.P. He, K.F. Yao, B.C. Wei, G.L. Chen, Metallographic analysis of Cu-Zr-Al bulk amorphous alloys with yttrium addition, Scr. Mater. 54 (2006) 1351–1355.
[26] W. Wang, Roles of minor additions in formation and properties of bulk metallic glasses, Prog. Mater. Sci. 52 (4) (2007) 540–596.
[27] A.L. Greer, Y.Q. Cheng, E. Ma, Shear bands in metallic glasses, Mater. Sci. Eng. Rep. 74 (4) (2013) 71–132.
[28] D. Sopu, A. Stukowski, M. Stoica, S. Scudino, Atomic-level processes of shear band nucleation in metallic glasses, Phys. Rev. Lett. 119 (19) (2017) 195503.
[29] R. Maaß, J.F. Löffler, Shear-band dynamics in metallic glasses, Adv. Funct. Mater. 25 (16) (2015) 2353–2368.
[30] M.B. Harris, L.S. Watts, E.R. Homer, Competition between shear band nucleation and propagation across rate-dependent flow transitions in a model metallic glass, Acta Mater. 111 (2016) 273–282.
[31] L. Wang, Z.P. Lu, T.G. Nieh, Onset of yielding and shear band nucleation in an Au-based bulk metallic glass, Scr. Mater. 65 (9) (2011) 759–762.
[32] M. Gao, C. Kursun, J.H. Perepezko, Unraveling structural relaxation induced ductile-to-brittle transition from perspective of shear band nucleation kinetics in metallic glass, J. Alloy. Compd. 952 (2023) 170022.
[33] J.Q. Wang, J.H. Perepezko, Focus: Nucleation kinetics of shear bands in metallic glass, J. Chem. Phys. 145 (21) (2016) 211803.
[34] M. Gao, J.H. Perepezko, Trimodal shear band nucleation distribution in a Gd-based metallic glass via nanoindentation, Mater. Sci. Eng. A 801 (2021) 140402.
[35] C.B. Jin, Y.Z. Wu, J.N. Wang, F. Han, M.Y. Tan, F.C. Wang, J. Xu, J. Yi, M.C. Li, Y. Zhang, J.T. Huo, J.Q. Wang, M. Gao, Nanoscale viscoelastic transition from solid-like to liquid-like enables ductile deformation in Fe-based metallic glass, J. Mater. Sci. Technol. 194 (2024) 63–74.
[36] D.V. Louzguine-Luzgin, M. Ito, S.V. Ketov, A.S. Trifonov, J. Jiang, C.L. Chen, K. Nakajima, Exceptionally high nanoscale wear resistance of a Cu47Zr45Al8 metallic glass with native and artificially grown oxide, Intermetallics 93 (2018) 312–317.
[37] F. Hu, Q. Luo, B. Shen, Thermal, magnetic and magnetocaloric properties of FeErNbB metallic glasses with high glass-forming ability, J. Non-Cryst. Solids 512 (2019) 184–188.
[38] X. Xu, L.Y. Chen, G.Q. Zhang, L.N. Wang, J.Z. Jiang, Formation of bulk metallic glasses in Cu45Zr48−xAl7Rex (Re = La, Ce, Nd, Gd and 0 ≤x≤ 5 at%), Intermetallics 15 (8) (2007) 1066–1070.
[39] L. Deng, B. Zhou, H. Yang, X. Jiang, B. Jiang, X. Zhang, Roles of minor rare-earth elements addition in formation and properties of Cu–Zr–Al bulk metallic glasses, J. Alloy. Compd. 632 (2015) 429–434.
[40] B.W. Zhou, W. Zhang, X.G. Zhang, H. Kimura, A. Makino, A. Inoue, Formation and thermal stability of Cu-based metallic glasses with high glass-forming ability, Metall. Mater. Trans. A 43 (8) (2011) 2592–2597.
[41] A. Takeuchi, A. Inoue, Classification of bulk metallic glasses by atomic size difference,heat of mixing and period of constituent elements and its application to characterization of the main alloying element, Mater. Trans. 46 (12) (2005) 2817–2829.
[42] M.Z. Xia, S.G. Ma, C.L. Li, J. Guo, Evaluation of glass-forming ability for metallic glasses based on order-disorder competition, Appl. Phys. Lett. 89 (2006) 091917.
[43] X.K. Xi, D.Q. Zhao, M.X. Pan, W.H. Wang, Y. Wu, J.J. Lewandowski, Fracture of brittle metallic glasses: brittleness or plasticity, Phys. Rev. Lett. 94 (12) (2005) 125510.
[44] R.T. Qu, Z.F. Zhang, Compressive fracture morphology and mechanism of metallic glass, J. Appl. Phys. 114 (19) (2013) 193504.
[45] J.H. Perepezko, S.D. Imhoff, M.W. Chen, J.Q. Wang, S. Gonzalez, Nucleation of shear bands in amorphous alloys, Proc. Natl. Acad. Sci. U. S. A. 111 (11) (2014) 3938–3942.
[46] L. Gu, L. Xu, Q. Zhang, D. Pan, N. Chen, D.V. Louzguine-Luzgin, K.F. Yao, W. Wang, Y. Ikuhara, Direct in situ observation of metallic glass deformation by real-time nano-scale indentation, Sci. Rep. 5 (2015) 9122.
[47] Y. Sato, S. Shinzato, T. Ohmura, T. Hatano, S. Ogata, Unique universal scaling in nanoindentation pop-ins, Nat. Commun. 11 (1) (2020) 4177.
[48] W.H. Wang, The elastic properties, elastic models and elastic perspectives of metallic glasses, Prog. Mater. Sci. 57 (3) (2012) 487–656.
[49] M.D. Demetriou, J.S. Harmon, M. Tao, G. Duan, K. Samwer, W.L. Johnson, Cooperative shear model for the rheology of glass-forming metallic liquids, Phys. Rev. Lett. 97 (6) (2006) 065502.
[50] M. Gao, J.H. Perepezko, Mapping the viscoelastic heterogeneity at the nanoscale in metallic glasses by static force spectroscopy, Nano. Lett. 20 (10) (2020) 7558–7565.
[51] F. Spaepen, Homogeneous flow of metallic glasses: a free volume perspective, Scr. Mater. 54 (3) (2006) 363–367.
[52] L. Li, E.R. Homer, C.A. Schuh, Shear transformation zone dynamics model for metallic glasses incorporating free volume as a state variable, Acta Mater. 61 (9) (2013) 3347–3359.
[53] B.W. Zhou, L. Deng, X.G. Zhang, W. Zhang, Enhancement of glass-forming ability and plasticity of Cu-rich Cu–Zr–Al bulk metallic glasses by minor addition of Dy, J. Mater. Res. 29 (12) (2014) 1362–1368.
[54] B. Huang, H.Y. Bai, W.H. Wang, Unique properties of CuZrAl bulk metallic glasses induced by microalloying, J. Appl. Phys. 110 (12) (2011) 123522.